ELSEVIER

Journal of Fluids and Structures 26 (2010) 339–358

JOURNAL OF FLUIDS AND STRUCTURES

www.elsevier.com/locate/jfs

Oscillatory motions of a prestrained compliant membrane caused by fluid–membrane interaction

M. Molki[a,*], K. Breuer[b]

[a]*Department of Mechanical Engineering, Southern Illinois University Edwardsville, Edwardsville, IL 62026-1805, USA*
[b]*Division of Engineering, Brown University, Providence, RI 02912, USA*

Received 29 July 2008; accepted 11 November 2009
Available online 12 February 2010

Abstract

Flow over a compliant membrane is a complex problem where the interaction between fluid and membrane determines the nature of the aerodynamic characteristics of the membrane wing. This investigation is concerned with the deformation and oscillatory motion of a membrane under aerodynamic loading. The approach is computational, but the analytical solution is also presented for a constant pressure loading. The computational results are compared with the experimental data available in the literature as well as with the present analytical solution. In this study, the values of Reynolds number are 38 416 and 141 500, and the angle of attack and prestrain range from 10° to 40° and from 0 to 0.074, respectively. This range of parameters makes the outcome of the investigation more relevant to applications involving the flight of micro air vehicles and the membrane wings of flying mammals such as bats. The computations indicate a mostly asymmetric deflection with the point of maximum camber located nearly at 40% of the chord length from the leading edge. The deflection is decreased with prestrain, and it is increased with Reynolds number. Moreover, the lift coefficient generally increases with the angle of attack. However, for $Re = 141\,500$, it increases first to a peak at 20–30° angle of attack, and then decreases. The drag coefficient is much higher than that of conventional airfoils. The membrane oscillates in the streamwise and vertical directions. The largest amplitude of oscillations is observed at 40° for $Re = 38\,416$. The oscillations are caused by the oscillatory nature of the flow due to fluid–membrane interaction and the formation of the leading edge and trailing edge vortices. Compared with a rigid membrane of the same camber, the compliant membrane has a smaller recirculation region which may lead to a delayed stall.

Keywords: Flexible membrane; Deflection; Vortex; Prestrain; Oscillation

1. Introduction

The interaction between a compliant membrane, such as a latex sheet mounted on a wire frame, and a flow field is more complex than that observed in flow over rigid objects. A horizontally positioned membrane is in an unstable state and may deflect either upward or downward. Under a positive angle of attack, however, the fluid stresses deflect the membrane upward. The deflection, in turn, affects the flow field and brings about a new stress distribution over the

*Corresponding author.
E-mail address: mmolki@siue.edu (M. Molki).

0889-9746/$ - see front matter © 2009 Elsevier Ltd. All rights reserved.
doi:10.1016/j.jfluidstructs.2009.11.003

Nomenclature

AR	arbitrary region
BL	boundary layer
c_d	drag coefficient, $(F_d/L)/(0.5\rho U^2)$
c_l	lift coefficient, $(F_l/L)/(0.5\rho U^2)$
E	modulus of elasticity, 0.9 MPa
f	frequency, Hz
F	body force, N
L	chord length, m
n	unit normal vector
p	fluid static pressure, Pa
Re	Reynolds number, $\rho UL/\mu$
s	length of the deformed membrane; also arc length, m
S	surface of AR, m^2
St	Strouhal number, fL/U
t	membrane thickness, m
t	unit tangent vector
T	membrane tension, N/m
T_0	membrane pretension, N/m
u	velocity component in x-direction, m/s
U	free-stream air velocity, m/s
v	velocity component in y-direction, m/s
v_i	velocity component, $v_1 = u$, $v_2 = v$
V	volume, m^3
w_j	membrane velocity, m/s
w	membrane maximum camber, m
x	Cartesian coordinate along the chord
$x_i(s)$	position vector for a point on the membrane
y	Cartesian coordinate perpendicular to the chord

Greek symbols

α	angle of attack, degree
Δp	pressure difference across the membrane, Pa
ε	strain
ε_o	membrane prestrain, $T_o/(Et)$
κ	membrane curvature, 1/m
μ	fluid viscosity, kg/ms
ν	fluid kinematic viscosity, m^2/s
ρ	density, kg/m^3
σ	membrane stress, T/t, Pa; standard deviation
τ_{ij}	fluid stress tensor
∂_i	partial derivative, $\partial/\partial x_i$
∂_o	time derivative, $\partial/\partial t$

Subscripts

i	free index, $i = 1, 2$ indicates x, y components
j	free index, $j = 1, 2$ indicates x, y components
max	maximum value

membrane and alters the original deformation. These dynamic fluid–solid interactions are absent when a rigid object is exposed to a flow field.

The present investigation is motivated by an ongoing research project at Brown University where a multidisciplinary team of engineers and biologists are investigating the aerodynamics and mechanics of bat flight. Bats have a flexible and compliant membrane wing that enables them to enjoy extraordinary flight capabilities (Hedenstrom et al., 2007). Although the Brown University project is primarily an experimental effort in which live bats and latex membrane models are tested in a wind tunnel, the aim of the present work is to predict the response of compliant membranes to airflow by a computational approach. As will be explained later in this paper, the computations performed here are based on a combination of computer programming developed in-house and the use of a commercial code. Because the membrane is compliant and deforms in response to airflow, a deforming mesh was used for the computations to accommodate the motion of the membrane. In addition to the computational approach, certain aspects of the problem are also examined analytically. The membrane equation is derived mathematically for a general case, and it is simplified to the form used in this work. The simplification of the general equation clearly shows all the assumptions made in obtaining the simplified equation. Although various versions of the membrane equation have been used by other investigators (Liang et al., 1997; Smith and Shyy, 1996; Perry and Chong, 1980), the general equation developed here, and the subsequent analytical solution, seems to be missing in the published literature.

Review of the literature indicates a limited number of studies on fluid–membrane interactions. Smith and Shyy (1996) performed computations to study the aerodynamics of a flexible membrane airfoil in turbulent flow. The angle of attack was 8° or lower and the Reynolds number was 1.3×10^6. They reported the membrane profile and the lift, tension, and moment coefficients. Greenhalgh and Curtiss Jr. (1986) performed experiments to study the aerodynamics of flexible membrane wings of triangular, parabolic, and elliptic shapes. The test wings were made of thin sheet metals that were flexible to some extent, but not so flexible to be fully compliant to the airflow. Liang et al. (1997) employed finite-element method to determine the fluid–membrane interaction in a channel flow where a membrane made a portion of one wall. Experimental efforts of Galvao et al. (2006) and Song and Breuer (2007) were intended to model membrane wings of flying mammals such as bats. The test membranes were made of latex sheet held in place by two parallel rods, positioned upstream and downstream, to form a low aspect-ratio wing. They were tested in wind tunnel at the lower

range of Reynolds number to simulate the aerodynamics of membrane wings of flying bats. These two investigations are the closest experimental counterparts of the present research. Also closely related to the present investigation are the experimental work of Rojratsirikul et al. (2008) and computations of Gordnier (2008), which discuss deflection, flow field, and modes of vibration of a membrane positioned in airflow under an angle of attack. Hedenstrom et al. (2007) focused on the transient vortex wake as the aerodynamic footprint of the bat flight. They showed that each membrane wing of the bat species generates its own vortex loop. They further reported negative and positive lift on different parts of the same membrane wing during the upstroke.

A more recent aerodynamic application involving fluid–membrane interaction is in the design of micro air vehicles (MAV) (Shyy et al., 2005; Hein and Chopra, 2007; Lian and Shyy, 2005). MAVs utilize membrane material for their flexible wings. They are designed for flights at low Reynolds numbers and have a short wing span. The wing, however, is thicker than the very thin membrane used in the present work. In contrast with the MAV applications, which are limited to lower range of Reynolds number, Mateescu (2003) presents a membrane solution at supersonic flows using an enhanced Lagrangian method.

The focus of the present research is on deformation and oscillation of a prestrained compliant membrane. The model employed in this work considers a latex membrane with properties and dimensions similar to that used in the experiments of Galvao et al. (2006) and Song and Breuer (2007). The experiments are intended to provide a simple model for membrane wings of flying bats, and the present computational work closely simulates these experiments. Later in this paper, we will make several comparisons with the experimental data. It is noteworthy that, although other investigators have studied some aspects of the membrane deformation and oscillation, the effect of prestraining a compliant membrane on deformation and oscillation for this range of Reynolds number is missing in the published literature. Further, we present a general equation for membranes, an analytical solution of the simplified equation, and the vorticity field for airflow over a dynamically deforming membrane under angle of attack. Furthermore, our computations demonstrate that the size of separation and recirculation region of a flexible membrane is smaller than that for a rigid membrane of the same camber, as confirmed by the experimental work of Rojratsirikul et al. (2008).

2. Mathematical equation of the membrane

The schematic of membrane is shown in Fig. 1. The leading edge is located at $(x,y) = (0,0)$, and the trailing edge is at $(x,y) = (L,0)$, where L is the chord length. The initial position of the undeformed membrane is horizontal; but the main flow approaches the membrane from below at an angle of attack denoted by α.

The arbitrary control region (AR), shown by dashed lines, embraces the membrane. The unit normal vector, **n**, unit tangent vector, **t**, and the membrane tension, T, are also shown. Applying the integral form of the conservation of momentum (Panton, 2005) to the arbitrary region, AR,

$$\partial_o \int_{AR} \rho v_i dV + \int_{AR} \rho n_j (v_j - w_j) v_i dS = \int_{AR} n_j \tau_{ij} dS - \int_{AR} n_i p dS + \int_{AR} \rho F_i dV + \oint T t_i ds, \tag{1}$$

where ∂_o is the partial derivative with respect to time, ρ the fluid density, v_i the fluid velocity, w_j the membrane velocity, τ_{ij} the viscous stress tensor, p the fluid pressure, and F_i the body force. We allow the top, T, and bottom, B, regions shown in the figure to shrink and to approach the membrane. Thus the fluid volumes in these regions vanish, and the AR coincides with the volume of the membrane. Now we make a number of assumptions to simplify Eq. (1). First, it is

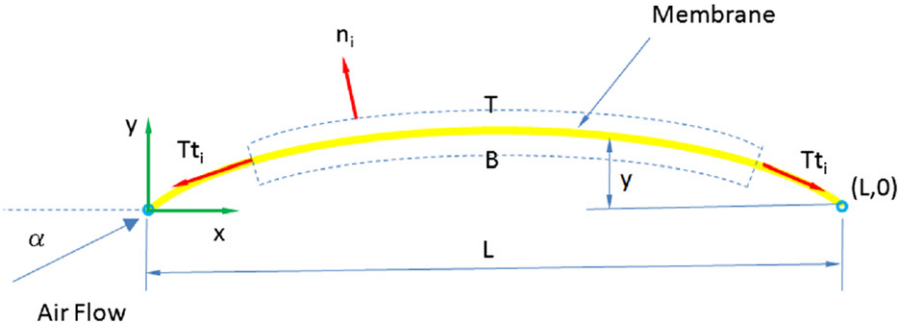

Fig. 1. Schematic of the deflected membrane under angle of attack. Chord line is horizontal; flow approaches the membrane from left. The membrane is fixed at the end points.

assumed that the membrane thickness is negligible, and thus the first integral on the left and the third integral on the right (the body force) drop from Eq. (1). Further, we assume that the membrane is impermeable, and the second integral on the left vanishes. The last integral on the right involving membrane tension may be written as

$$\oint Tt_i ds = \int [\partial_i T - n_i n_j \partial_j T - 2\kappa T n_i] dS, \tag{2}$$

where the integrand on the right side of Eq. (2) is composed of the gradient of membrane tension, $\partial_i T$, minus the component of gradient normal to the surface, minus $2\kappa T n_i$, with κ being the membrane curvature.

Substituting Eq. (2) into Eq. (1), collecting terms, and setting the integrand equal to zero, we have

$$(n_i \tau_{ijB} - n_j p_B) - (n_i \tau_{ijT} - n_j p_T) - (\partial_j T - n_j n_i \partial_i T) - 2\kappa T n_j = 0. \tag{3}$$

It is further assumed that flow is two-dimensional and membrane deflection is small (small curvature) compared to the chord length, L, and thus the unit vector normal to the membrane may be approximated as $n_j = (0,1,0)$. Therefore, Eq. (3) for $j = 1$ (x-direction) and $j = 2$ (y-direction) is simplified to

$$(\tau_{21B} - \tau_{21T}) - \partial_1 T = 0, \tag{4}$$

$$(\tau_{22B} - p_B) - (\tau_{22T} - p_T) - 2\kappa T = 0. \tag{5}$$

Furthermore, assuming that the viscous stresses represented by Eqs. (4) and (5) are negligible, Eq. (4) indicates that the tension of the membrane is constant in the x-direction. With this assumption, Eq. (5) simplifies to

$$(p_T - p_B) - 2\kappa T = 0. \tag{6}$$

Membrane curvature may be expressed as (Kreyszig, 1991)

$$\kappa = \sqrt{\ddot{x}_i(s) \cdot \ddot{x}_i(s)} = \left(\frac{d^2 y}{dx^2}\right) \Bigg/ \left[1 + \left(\frac{dy}{dx}\right)^2\right]^{3/2}, \tag{7}$$

where $x_i(s)$ is the position vector for a point on the membrane, s the arc length along the membrane, and $\ddot{x}_i(s) = d^2 x_i / ds^2$. For small deflections, $(dy/dx)^2$ may be neglected on the right hand side of Eq. (7). To justify this assumption, for 10% parabolic deflection, the mean slope of the membrane is $dy/dx = 2y_{\max}/L = 2(0.1) = 0.2$ and the denominator on the right-hand side of Eq. (7) is $[1+(dy/dx)^2]^{3/2} = [1+(2y_{\max}/L)^2]^{3/2} = 1.06$, indicating only 6% difference when the aforementioned term is dropped from Eq. (7). Therefore, it is further assumed that the membrane curvature is approximately $\kappa = d^2 y / dx^2$. With the foregoing assumptions, the membrane equation, Eq. (6), may be written as

$$\frac{d^2 y}{dx^2} = -\frac{\Delta p}{T + T_o}, \tag{8}$$

where $\Delta p = p_B - p_T$ is the pressure difference across the membrane and T_o is the pretension of the membrane. Since the pressure difference comes from the flow field, and it varies with time, Eq. (8) is time-dependent via the pressure difference term. The initial condition for this equation is to have no deflection, i.e., $y = 0$, for the entire length of the membrane. Boundary conditions for Eq. (8) are $y = 0$ at the two ends of the membrane, namely, at the membrane leading edge $(x,y) = (0,0)$ and at the membrane trailing edge $(x,y) = (L,0)$. In the present investigation, it is assumed that the equation governing the deformation of the membrane is Eq. (8).

The membrane tension, T, in Eq. (8) is determined from a linear stress–strain relation, namely $\sigma = E\varepsilon$, where $\sigma = T/t$ and ε are stress and strain due to cambering deformation of the membrane. In these relations, t and E are, respectively, the membrane thickness and modulus of elasticity. The membrane strain is found from the length of the cambered membrane and the chord as $\varepsilon = (s - L)/L$, where s is the length of the deformed membrane. Substituting for membrane length, the tension corresponding to ε is

$$T = tE\varepsilon = tE\left\{\frac{1}{L}\int_0^L [1 + (dy/dx)^2]^{0.5} dx - 1\right\}. \tag{9}$$

The pretension, T_o, is related to the prestrain of the membrane as $\varepsilon_o = T_o/(Et)$. The prestrain appears as a major parameter throughout this paper. Eqs. (8) and (9) complete the mathematical formulation of the membrane deformation. The two equations are linked via membrane tension, and they are solved simultaneously to obtain the deformation of the membrane.

3. Analytical solution for constant pressure loading

Eq. (8), together with its companion Eq. (9), may be solved analytically when the pressure difference across the membrane, Δp, is constant. The analytical solution will later be compared with the present computations.

The extent of membrane deformation depends on the magnitude of pressure loading. For a fixed pressure loading, and thus a fixed membrane deformation, the tension will remain constant throughout the membrane. Integrating Eq. (8), assuming the right–hand side to be constant, and applying the two boundary conditions, we obtain

$$\frac{y}{L} = -\alpha\left(\frac{x}{L}\right)\left(\frac{x}{L}-1\right) \tag{10}$$

where $\alpha = (\Delta pL/2)/(T+T_o)$. Substituting dy/dx from this equation into Eq. (9) and carrying out the integration, we obtain the following expression for membrane tension:

$$T = tE\left\{-\frac{1}{4\alpha}\left[-2\alpha\sqrt{\alpha^2+1}-2\sinh^{-1}\alpha\right]-1\right\}. \tag{11}$$

This is an implicit solution for membrane tension, as T appears on both sides of the equation (α depends on T). The equation is solved iteratively to obtain membrane tension, which is then substituted in Eq. (10) to obtain membrane camber. This completes the analytical solution of the membrane equation for the constant pressure loading.

4. Formulation of the flow field

The flow field is governed by the continuity and momentum equations. For unsteady laminar flow of an incompressible Newtonian fluid, we have

$$\partial_i v_i = 0, \tag{12}$$

$$\partial_o v_i + v_j\partial_j v_i = -(1/\rho)\partial_i p + \nu\partial_j\partial_j v_i. \tag{13}$$

The initial condition is $u(x,y,0) = U_x$ and $v(x,y,0) = 0$. Boundary conditions are $u = U_x = U\cos\alpha$, $v = U_y = U\sin\alpha$ at the left (inlet) boundary, $du/dy = 0$ and $v = 0$ on the top and bottom boundaries, and zero gradients (pressure outlet) at the right (outlet) boundary of the solution domain. Here, U_x and U_y are the horizontal and vertical components of the free-stream velocity U, and α is the angle of attack. It is to be noted that the initial position of the undeformed membrane is horizontal and the free-stream makes an angle α with the horizontal chord line. The complete mathematical formulation of the fluid-membrane problem is thus comprised of Eqs. (8), (9) and (12), (13) and the stated initial and boundary conditions.

The present problem is strongly influenced by the interaction between flow and membrane. Flow over the membrane, establishes the pressure difference across the membrane; while the membrane deflection alters the flow and pressure fields. Thus, the aforementioned equations are solved as follows. First, the flow field is solved to obtain the pressure distribution over and under the membrane. Using these pressures, the membrane equation is solved to obtain the membrane deflection. The deflection is subsequently used to move the grid points located on the membrane as well as those near the membrane. With this new shape of the deflected membrane, the flow equations are again solved to find a new pressure difference across the membrane. This cycle of computations is continued until the initial transients are damped out and a repeatable flow pattern is emerged.

The computational method employed to solve these equations is discussed in the following section.

5. The computational approach

A *C* program has been developed and linked to a commercial software to solve the governing equations of this problem. The *C* program solves the membrane Eqs. (8–9) using finite differences. Eqs. (12) and (13) are solved by the commercial software Fluent. The *C* program is linked to Fluent as a User Defined Function (UDF) to communicate the

membrane information with the software. The UDF contains a number of macros that are recognized by the commercial software and it facilitates the communication between the membrane solution (from the *C* program) and the commercial software.

As seen in Eqs. (12) and (13), the flow is assumed to be laminar and unsteady. At the low values of Re considered in this investigation, flow is predominantly laminar and the presence of any possible pockets of turbulence is ignored. At higher values of Re, turbulence may occur and a possible choice for turbulence model is the k–ω model which enables a low-Re correction to the turbulent viscosity to account for the transitional flow.

Membrane Eqs. (8) and (9) are discretized on a uniform mesh using central differences to allow a second-order accurate solution. The commercial software, however, is based on a finite-volume method which also handles an unstructured and deforming mesh. Mesh deformation is a vital feature for the present problem in which the flexible membrane deforms and oscillates throughout the solution process.

The solution domain is 2.7 m × 2.7 m. The origin of the coordinate system is placed at the leading edge of the membrane. With this arrangement, the x (horizontal) and y (vertical) coordinates each range from −1.35 m at the domain inlet to +1.35 m at the outlet. The mesh is uniform on and around the membrane at the beginning of the computations. In all the computations, the undeformed membrane is 0.129 m long. In order to accommodate the mesh deformation and oscillation, two rectangular regions of equal size are considered, one above and one below the undeformed membrane. The size of these regions depends on the value of Reynolds number; they are 0.02 m × 0.129 m and 0.04 m × 0.129 m, respectively, for $\mathrm{Re} = UL/v = 38{,}416$ and 141,500. Here, U is the free-stream velocity and v is the kinematic viscosity of air ($v = \mu/\rho$, $\mu = 1.7894 \times 10^{-5}$ kg/ms, and $\rho = 1.225$ kg/m^3). Each region is meshed uniformly with 11,094 (for low Re) and 15,050 (for high Re) cells. In order to resolve the velocity gradients near the membrane surface, four rows of boundary layer mesh are applied to the membrane in these regions. The first layer of cells adjacent to the membrane surface is 0.1 mm thick in the direction perpendicular to the undeformed membrane for all cases. Outside these regions, the mesh is structured, but non-uniform, and it is clustered towards the membrane. With this arrangement, the computational meshes for the low and high values of Re have, respectively, 77 044 and 86 060 cells.

The runs for the lower Re are more stable and are performed with higher values of the relaxation factor. The pressure–velocity coupling is based on the PISO algorithm with skewness and neighbor corrections set equal to one. The relaxation factors for pressure and momentum are, respectively, 0.7 and 1. In contrast, the runs for the higher Re do not converge with such high values of relaxation factor. The pressure–velocity coupling in this case is achieved by using the SIMPLE algorithm. The relaxation factors for pressure and momentum are 0.3 and 0.7. In both PISO and SIMPLE, the velocity discretization is based on the second-order upwind scheme. In all cases, the unsteady approach is based on the first-order implicit scheme in time with a time step of 10^{-4} s. The computations in each time step converge with less than 20 iterations, often with about 5 to 10 iterations. The convergence criterion is to reduce the residuals of the continuity and momentum equations for each time step to below 10^{-4}.

At the onset of computations, the membrane is a straight line representing the initially undeformed state of the membrane. The membrane is positioned horizontal, but the mainstream entering the domain at $x = -1.35$ m approaches the membrane from below at a prescribed angle of attack. In this study, the computations are performed for the angles of attack of 10°, 20°, 30°, and 40°.

In a typical run, the velocities are initialized by the free-stream values. The membrane deformation, i.e. the (y) dependent variable in Eq. (8), is initialized to zero. As the computations progress, non-zero values of membrane deformation emerge from the solution, which require the neighboring mesh to deform accordingly. In the present work, the deforming mesh option of the commercial software is used to deform the mesh in the regions above and below the membrane. However, the amount of deformation is calculated in the *C* program at the end of each time step and is communicated with the commercial software. The mesh nodes located on the membrane move upward or downward exactly as dictated by the membrane motion. The nodes located in the two regions above and below the membrane, namely, between the membrane and horizontal lines located at $y = \pm 0.02$ m or ± 0.04 m (depending on Re), move progressively less as the y-coordinate of the node approaches the values $y = \pm 0.02$ m or ± 0.04 m. With this arrangement, the node displacement range from the maximum value at the membrane position to zero on the outer boundaries of the neighboring mesh regions.

The computations are carried out for 10 000 time steps (1 s) until the initial transients disappeared from the solution. They are continued for another 10 000 iterations for a total computation time of 2 s. During this total time with Re = 38,416, the free-stream travels 67.4 chord length and 3.2 solution domain length. For Re = 141 500, the corresponding travel lengths are 248.4 and 11.9. These values, together with the observations during the runs, ensure that the choice of 20 000 total iterations, corresponding to 2 s, is quite sufficient for the present computations.

6. Mesh refinement study and comparison with the analytical solution of the circular-arc airfoil

In this section, the effect of the location of boundaries and the density of the mesh on the computational solution is evaluated. In addition, the present method is applied to the inviscid flow over a circular-arc airfoil, which has an analytical solution. Furthermore, the present method will be tested with the analytical solution presented earlier in Eqs. (10) and (11)) wherein the pressure difference across the membrane is assumed to be constant.

Table 1 presents the lift and drag coefficients for total number of cells in the computational mesh. Two different domain sizes are considered; one is for a small domain, $0.5\text{ m} \times 0.3\text{ m}$, and the other is larger, $2.7\text{ m} \times 2.7\text{ m}$. Also shown in this table is the lift coefficient obtained from the analytical solution of Katz and Plotkin (2001) for inviscid flow over a circular-arc airfoil. This comparison is made for the maximum camber ratio (maximum ordinate to chord length, y_{max}/L) of 10% and the angle of attack of zero.

For the small domain, the lift coefficient increases to higher than the analytical value. Considering the fact that when the inlet boundary is closer to the membrane the flow imposes a higher fluid velocity on the membrane, the higher lift coefficient for the smaller domain is not unexpected. However, when the boundaries are moved away and the domain is larger, the lift coefficient is smaller than that obtained from the smaller domain. In this case, as the mesh is refined, the computational values improve and tend to approach the analytical solution asymptotically. For the finest mesh in this figure, the numerical solution for the inviscid flow over the circular arc is 1.25% below the analytical value.

Further comparison with the analytical solution of the inviscid flow over the circular-arc airfoil is presented in Fig. 2. The comparison is made between the analytical and computational results for fluid pressure, x-component of fluid velocity, and magnitude of the fluid velocity, all on the airfoil surface. These computations are performed on the larger domain of $2.7\text{ m} \times 2.7\text{ m}$. As is evident from the figure, the present method predicts the analytical solution very well. This also confirms that the larger domain is more suitable for the present computations. In fact, according to Shyy et al. (2007), for a domain of dimensions $10L \times 10L$ (L is the chord length), the computed lift, drag, and aerodynamic moment change less than 1% with the domain size. The domain used for the final computations of the present work is $2.7\text{ m} \times 2.7\text{ m}$, which corresponds to nearly $21L \times 21L$, and is much larger than the domain employed by Shyy et al. (2007).

The grid study is also conducted for viscous airflow over the membrane (Table 1). These results are obtained by the same computational tools, namely the commercial software and the C program, and for the same circular-arc airfoil, except that the fluid is air with density $\rho = 1.225\text{ kg/m}^3$, viscosity $\mu = 1.7894 \times 10^{-5}\text{ kg/ms}$, Re = 38 416, and the angle of attack of $\alpha = 0^\circ$. Also shown in the table are the values of $\pm 2\sigma$, which represent twice the standard deviation of the lift or drag coefficients. Two sets of data are seen in the table. Those with BL are obtained with a mesh which has

Table 1
Grid refinement study on circular-arc airfoil for inviscid and viscous fluids; $U_\infty = 3.35\text{ m/s}$, corresponding to Re = 38 416 for viscous fluid, and $\alpha = 0^\circ$.

Domain. (m × m)	No. of domain cells (no. of faces on membrane)	BL mesh	Fluid	Computed $C_l \pm 2\sigma$	Computed $C_d \pm 2\sigma$	Analytical C_l
0.5 × 0.3	17,100	No	Inviscid	1.270		1.257
0.5 × 0.3	28,990	No	Inviscid	1.278		1.257
0.5 × 0.3	49,470	No	Inviscid	1.283		1.257
0.5 × 0.3	111,872	No	Inviscid	1.286		1.257
2.7 × 2.7	50,904	No	Inviscid	1.186		1.257
2.7 × 2.7	74,688	No	Inviscid	1.235		1.257
2.7 × 2.7	102,152	No	Inviscid	1.240		1.257
2.7 × 2.7	146,610	No	Inviscid	1.241		1.257
2.7 × 2.7	72,000 (86)	No	Viscous	0.282 ± 0.078	0.0486 ± 0.0130	
2.7 × 2.7	112,000 (129)	No	Viscous	0.513 ± 0.168	0.0508 ± 0.0333	
2.7 × 2.7	148,000 (161)	No	Viscous	0.652 ± 0.147	0.0522 ± 0.0268	
2.7 × 2.7	79,000 (258)	No	Viscous	0.648 ± 0.158	0.050 ± 0.0287	
2.7 × 2.7	70,000 (86)	Yes	Viscous	0.231 ± 0.0451	0.0437 ± 0.0089	
2.7 × 2.7	112,000 (129)	Yes	Viscous	0.613 ± 0.145	0.0548 ± 0.0216	
2.7 × 2.7	148,000 (161)	Yes	Viscous	0.721 ± 0.124	0.0536 ± 0.0209	
2.7 × 2.7	81,000 (258)	Yes	Viscous	0.707 ± 0.133	0.0537 ± 0.0221	

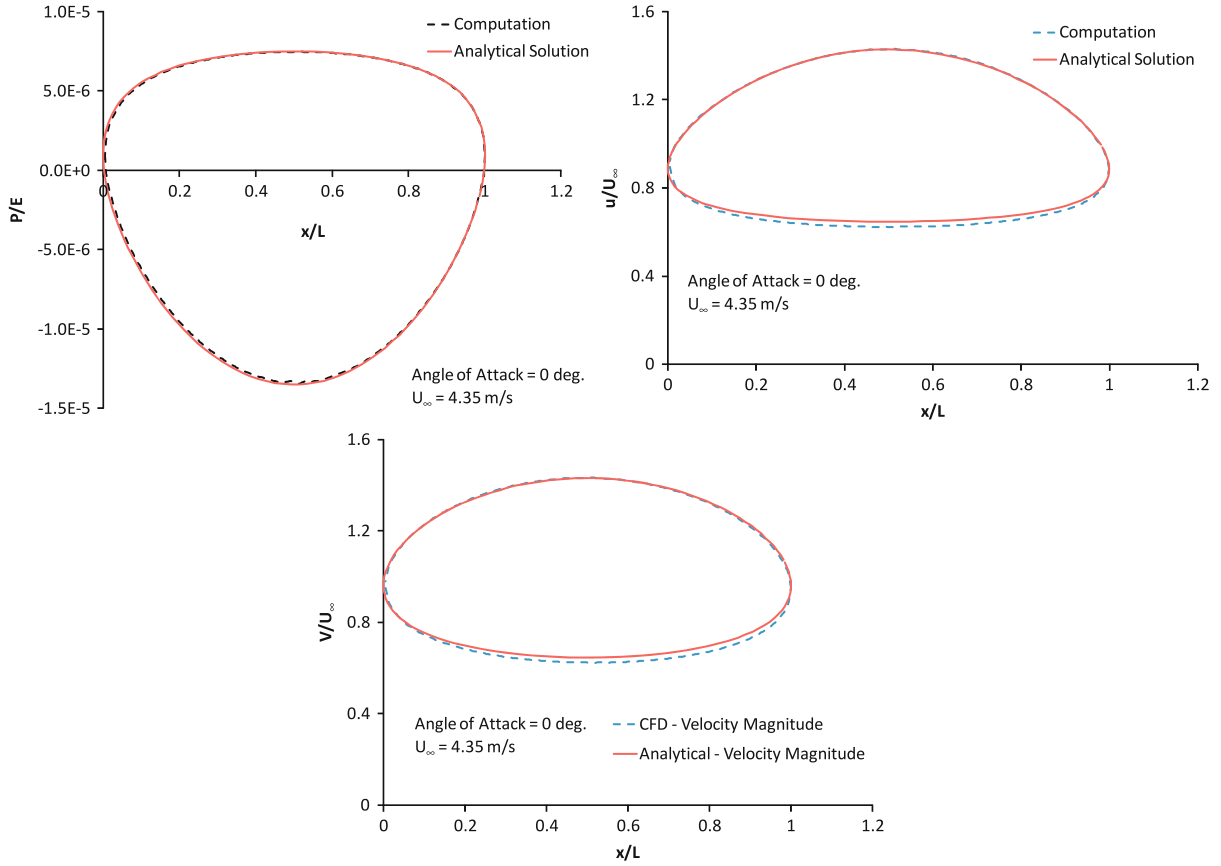

Fig. 2. Computational versus analytical solution for the inviscid flow over circular-arc airfoil with maximum camber ratio of 10%.

boundary layer mesh attached to both sides of the membrane to capture the steep gradients caused by the velocity no-slip boundary condition. The numbers inside parentheses in front of number of cells are number of faces on the membrane, i.e., number of grids on the membrane minus one.

Review of the values in Table 1 indicates that the data obtained with BL are generally higher than those without BL. The presence of the boundary layer mesh on the membrane should improve the computations. As the membrane mesh is refined, both lift and drag coefficients approach a limiting value. It is also found that larger number of faces on the membrane improves the computation. Based on these results, the final computations are performed on a mesh with 77 044 cells in the domain for Re = 38 416, and 86 060 cells for Re = 141 500, both with BL mesh attached to both sides of the membrane and with 258 faces on the membrane.

7. Comparison with the analytical solution of the membrane with constant Δp

The analytical solution of Eq. (8) for constant pressure difference across the membrane, Eqs. (10) and (11), is plotted in Fig. 3. The abscissa is aerodynamic load, represented by the pressure difference Δp divided by the modulus of elasticity of the membrane E, and the ordinate is the maximum camber ratio. The analytical solution is shown for different values of membrane prestrain $\varepsilon_o = T_o/(Et)$. The symbols shown in the figure are obtained from our computational results for airflow over the flexible membrane, i.e. from the solution of Eqs. (8) and (9), and (12) and (13). For the symbols, the ordinate is obtained from pressure difference across the membrane based on the averaged pressure over the membrane surface after 2 s of computational time, divided by the modulus of elasticity of the membrane $E = 0.9$ MPa.

As seen in Fig. 3, the analytical camber ratio increases with the loading. The rate of increase is faster for lower loadings. It is noteworthy that the right side of Eq. (8) for a membrane with no prestrain and no load is indeterminate,

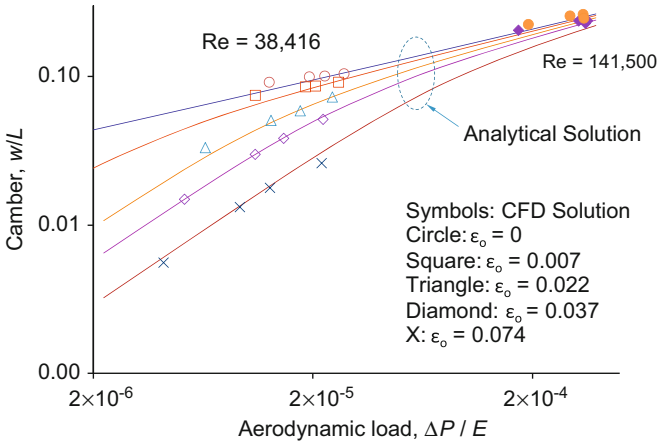

Fig. 3. Analytical solution (solid lines) for constant pressure difference across the membrane is compared with the computational results (symbols). The symbols are based on CFD solution of the Navier–Stokes equations. The solid lines are from the analytical solution using the pressure difference obtained from the computation.

and the membrane is in an unstable state. However, at the onset of the flow, even with a small angle of attack, a small pressure difference would develop across the membrane; at this state, the membrane is not strained yet and tension in the membrane is absent. In this case, the right-hand side of Eq. (8) is infinitely large, resulting in a rapid response of the membrane to the initial loading imposed by the flow. As the membrane deforms and larger tension develops, the right side of Eq. (8) decreases, leading eventually to an equilibrium state in which pressure and tension forces are balanced. At higher values of prestrain, the tension has already developed in the membrane and the camber ratio is smaller.

There are two groups of symbols in Fig. 3. The open symbols are for the lower flow speeds corresponding to Re = 38 416, while the solid symbols are for the higher speeds at Re = 141 500. The pressure distribution over the membrane surface, as obtained from the computations, is highly non-uniform; this is especially true for airflow at higher speeds. This leads to a pressure difference that is not uniform along the membrane. Despite the non-uniformity of pressure in the latter case, the trend and magnitudes of camber seen in the figure for the two methods agree quite well.

8. Results and discussion

In this section, the computational results will be presented and discussed. The results are comprised of membrane deflection, lift and drag coefficients, oscillatory motions of the membrane, vortex generation, and a comparison between flexible and rigid membranes.

8.1. Membrane deflection

Fig. 4 presents the deflection of the membrane for different values of prestrain for Re = 38 416 and 141 500, and for angles of attack of 10° and 40°. The abscissa is the dimensionless distance from the leading edge of the membrane, and the ordinate is the dimensionless deflection. The membrane prestrain appears as a parameter in this figure, ranging from 0 to 0.074. The points of maximum deformations are identified with solid square symbols attached to each deflection curve.

Review of the plots indicates that, for a given Reynolds number and angle of attack, the highest deflection occurs for the case with no prestrain. The deflection decreases as the prestrain is increased. The membrane is more sensitive and responsive to this parameter at lower values of prestrain. For instance, at 10° angle of attack, the values of $d(y/L)/d\varepsilon_o$ at the point of maximum deflection are 2.35 and 0.25, respectively, for the ranges $\varepsilon_o = 0$–0.007 and $\varepsilon_o = 0.037$–0.074; for 40° angle of attack, the respective values in the same ranges of prestrain are 1.82 and 0.68. This finding is consistent with the analytical solution presented earlier in Fig. 3 in which the slopes of the deflection curves are higher at lower loadings.

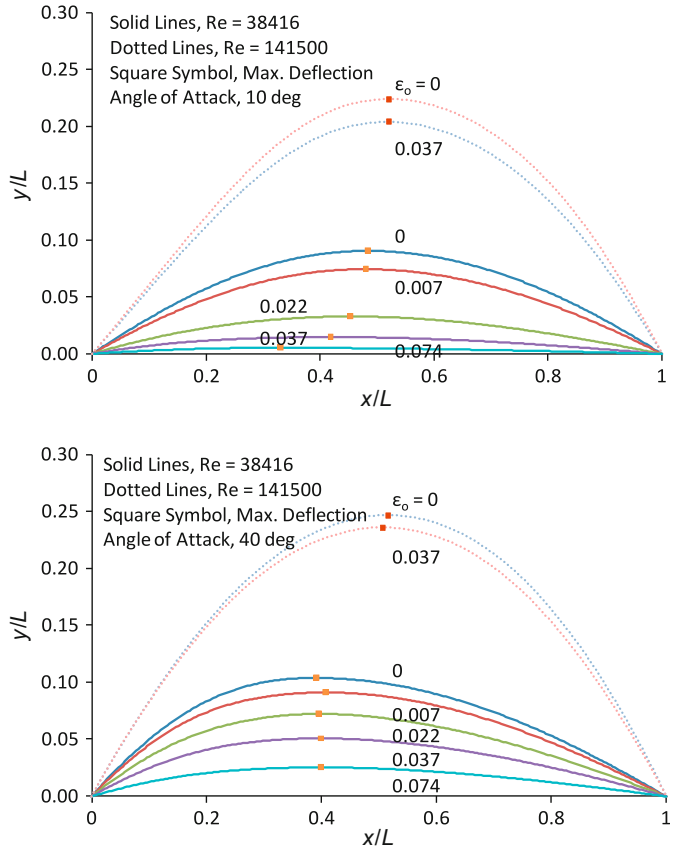

Fig. 4. Deflection of the prestrained membrane. The membrane deflection is nearly symmetric at higher values of Reynolds numbers. The symmetry is disturbed at higher pretensions.

The deflections are larger at higher Re. As Re increases, the aerodynamic loading on the membrane increases, resulting in higher deflections. Review of the data for Re = 141 500 shows that the membrane deflection is not as sensitive to prestrain as it is at lower values of Re. At 10° and 40° angles of attack, the values of $d(y/L)/d\varepsilon_o$ for the range of prestrain shown in the figure for this Re are 0.53 and 0.29, respectively. These values are lower than the respective values given earlier for Re = 38 416. At Re = 141 500, the membrane is already under a large aerodynamic load, and according to the analytical solution depicted in Fig. 3, it should be less sensitive to prestrain. The deformation changes seen in Fig. 4 for higher Re at ε_o of 0 to 0.037 is clearly smaller than that seen at lower Re.

Another observation in Fig. 4 is the lack of symmetry of deflections. The parameters that affect the asymmetry are Re, prestrain, and angle of attack. In the range of prestrain considered in this research, higher Re generally leads to more symmetric deformation. For instance, at the prestrain value of 0.037, the deformation for higher Re is nearly symmetric for both 10° and 40°, while the corresponding deformation at lower Re is quite asymmetric. Higher values of prestrain at lower Re lead to higher asymmetry. This does not appear true at higher Re, but there is not enough computational data to fully support this conclusion for higher Re. The experimental data of Rojratsirikul et al. (2008) shows that the maximum camber is located approximately at $x_{max}/L = 0.42$ to 0.5, which is close to the values of the present computation. Angle of attack also contributes to the asymmetry of the deformations as is evident from the figure. At 40°, the maximum deformation at lower Re occurs nearly at $x/L = 0.4$ for all values of prestrain.

8.2. Lift and drag coefficients

Lift and drag coefficients of the flexible membrane are presented in Fig. 5. The abscissa is the angle of attack, and Reynolds number and prestrain appear as parameters. Also shown in the figure are the experimental data of Galvao et al. (2006) for compliant membrane and rigid wing, and the lift coefficient of a rigid circular-arc airfoil (dashed lines)

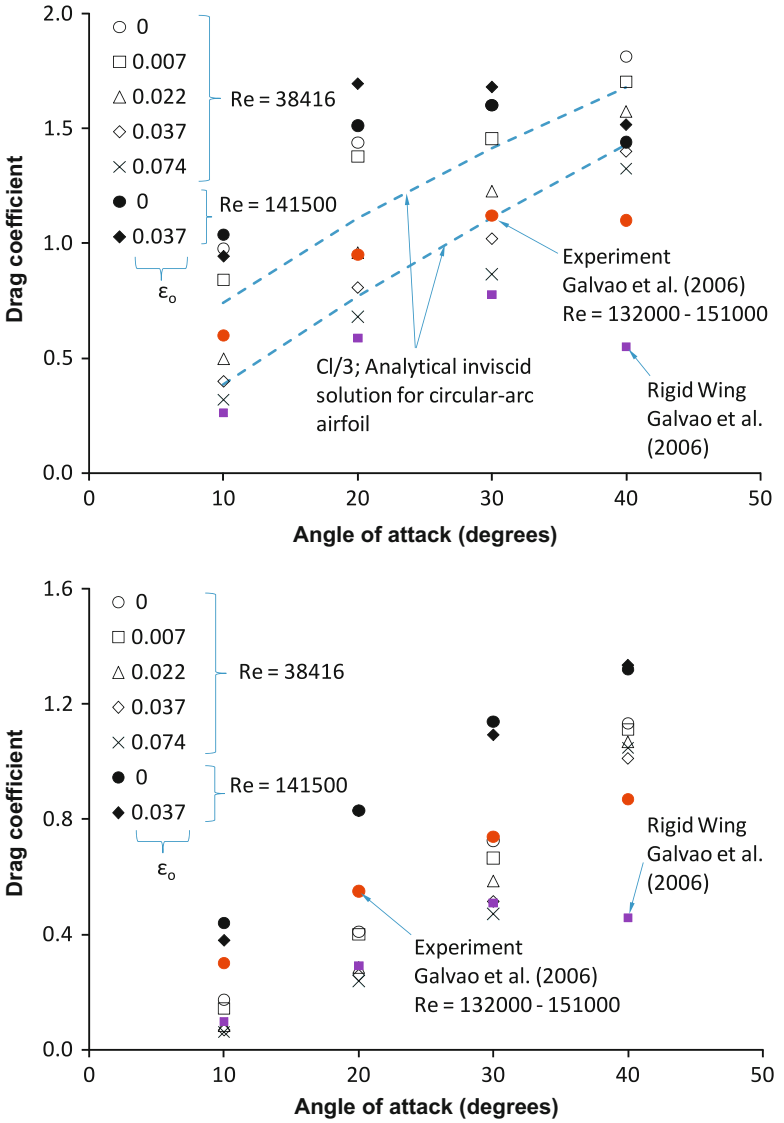

Fig. 5. Lift and drag coefficients of the flexible membrane versus angle of attack. The experimental data are from Galvao et al. (2006).

from the analytical solution of inviscid flow from Katz and Plotkin (2001). In order to accommodate the lift coefficient of the circular-arc airfoil in the plot, we have shown the lift coefficient as $c_l/3$ in the figure. The upper and lower dashed lines seen in the figure are obtained for the circular-arcs whose maximum camber ratio is the same as those of the flexible membranes of the present computations for the prestrain values of 0 and 0.074, respectively.

The range of Re of the experimental data, namely, 132 000–151 000, includes the value Re = 141 500 of the present computations. Therefore, the experimental data should be compared with the computations for Re = 141 500. Moreover, the membrane used in the experiments of Galvao et al. (2006) was mounted on the test frame taut, but not stretched. It is clear from the figure that both data and computation show a similar trend. The lift coefficient initially increases with the angle of attack. But near 30°, it begins to decrease. The largest experimental and computational value for the lift coefficient occurs around 30°, except for the computation for the prestrain value of 0.037 which peaks near 20°. Despite the similarity of trends, the computations overpredict the experimental data. Considering the fact that the membrane used in the experiment had a finite span and relatively small aspect ratio, the smaller lift could be due to the formation of tip vortices.

A noteworthy observation in Fig. 5 is that, at low angles of attack, the trend of circular-arc airfoil is very similar to the experimental data and the computational results. This is seen for both values of Re up to 20°. Beyond 20°, the data

and high-Re computations approach a peak point and then start to decrease, while the low-Re computations and the circular-arc airfoil continue with the same increasing trend. The circular-arc lift coefficient is based on the analytical solution of the inviscid flow and is, therefore, free from flow separation which may lead to stall in real airfoils. Furthermore, since the viscosity is absent in the circular-arc result, this flow is equivalent to a flow with infinitely large Reynolds number. As such, it is seen that the magnitude of the computed results follow the correct order with respect to Re, and the lift coefficient of the circular-arc obtained from inviscid flow has the highest value.

The drag coefficients shown in Fig. 5 are much larger than those seen for the conventional streamlined bodies such as airfoils. This is due to the membrane camber and oscillations that continuously impart kinetic energy to the fluid and thus impose a higher resistance to the flow. Comparing the experimental data with the computational values at Re = 141 500, it is seen that the computations overpredict the data, as it was also seen for the lift coefficient. However, their lift to drag ratio is closer; for 10° to 40°, the range of lift-to-drag ratio is 2.0–1.3 for the experimental data, 2.4–1.1 for the computation with zero prestrain, and 2.5–1.1 for the computation with 0.037 prestrain. The differences between the data and computation could be due to the tip vortices that tend to reduce the lift coefficient, and in consequence, to lower the membrane camber and its subsequent resistance to the airflow, leading to a lower drag coefficient. The trends of the drag coefficient for the data and computations are similar, except for the slope of the data which is somewhat smaller.

In order to examine the performance of the compliant membrane, the experimental data of Galvao et al. (2006) for rigid wing are also shown in the figure. The rigid wing is a flat steel plate that was tested at different angles of attack. It is clear from the figure that the compliant membrane has higher lift coefficient than the rigid wing. This is true even for the highest prestrain value of 0.074 considered in the computations at low Re. For a given angle of attack, the lift coefficient is approximately proportional to the camber. This provides a mechanism for a variable lift coefficient for compliant membranes, which in the case of mammalian or bat flight, are able to improve their lift characteristics under variable flight conditions. The drag coefficient of the rigid plate, however, is lower. It appears that the higher cambers that result in higher lift coefficient also increase the drag coefficient.

8.3. Oscillatory motion of the membrane

The oscillatory motion of the membrane is presented in Fig. 6. The abscissa is the location of the maximum camber as the streamwise distance from the leading edge, and the ordinate is the dimensionless maximum camber ratio. In this plot, the angle of attack, the prestrain, and Re appear as parameters. In order to avoid a crowded plot, only the extreme values of parameters are considered, namely, $\alpha = 10^\circ$ and 40° and the extreme ε_o values for the two Re. These oscillations are obtained from a 2-D model assuming no mass for the membrane material, i.e., no inertia term in the membrane equation.

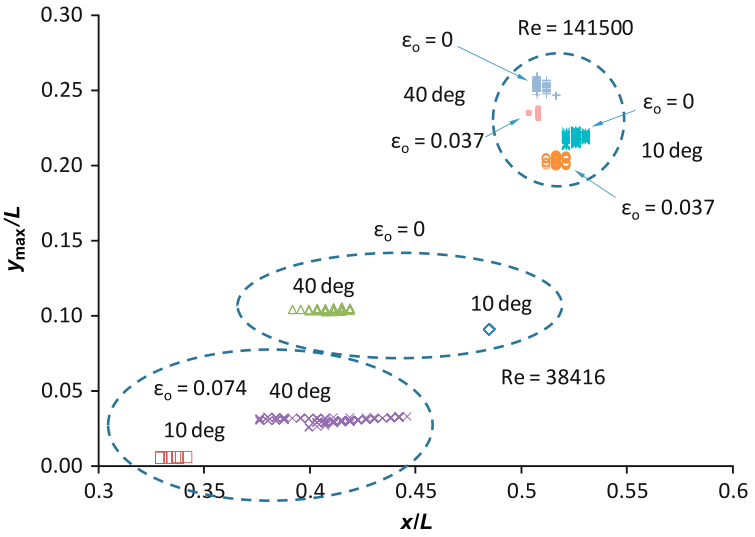

Fig. 6. Oscillatory motion of the maximum camber point of the membrane. The primary oscillation is in the horizontal direction. The lower Re shows higher oscillations.

It is seen from the figure that the point of maximum camber on the membrane moves in the vertical and streamwise directions. However, the high-Re oscillations have a narrow range of amplitudes. The computational points for this case are gathered in a small neighborhood near the middle ($x/L = 0.5$) of the membrane. For the lower Re, on the other hand, there are two distinct groups of points labeled based on the value of prestrain. The largest oscillations are observed for the membrane with the prestrain value of 0.074 at 40° angle of attack. In this case, the oscillations are predominantly streamwise with small vertical oscillations. The next to the largest oscillation corresponds to the prestrain value of zero at the lower Re for the same 40° angle of attack. It is quite surprising that the largest amplitude of oscillations corresponds to the highest value of prestrain; but it is not unexpected to have these large oscillations when the angle of attack is 40°. As will be discussed shortly, the flow field for the higher angles of attack is more complex and has multiple vortices with frequent vortex shedding.

The physical basis for this observation that low values of Re show larger amplitude oscillations may be explained by considering two major factors that affect the amplitude of oscillation. One factor is related to the flow field and the other one is due to the membrane tension. At higher Re, it is expected to see more intense vortex shedding and larger pressure variation across the membrane. On the other hand, the tension increases with Re and tends to make the membrane less responsive to the flow-induced pressure fluctuations. At low tensions, as is also seen in the analytical solution, the membrane is more sensitive to pressure fluctuations and responds rapidly to the flow conditions. It appears that at higher Re, the inhibiting effect of higher tension is dominant; thus the amplitude of fluctuations is smaller.

In order to provide frequencies of the unsteady membrane deflection, eight control points were placed inside the computation domain—four in the fluid and four on the membrane. The points on the membrane were at the streamwise locations corresponding to the points situated in the fluid. Velocity and membrane deflection at these control points were recorded during the computations and, using fast Fourier transform, power spectrums of the recorded values were obtained as shown in Fig. 7. In this figure, the left plots are for the fluid points and the right plots are for the points located on the membrane. The fluid points are located at (a) $(x/L,y/L) = (0.147,0.112)$, (b) (0.271,0.152), (c) (0.5,0.191), and (d) (0.748,0.184). The four membrane points were on the membrane at the same x/L locations as the fluid points.

Review of the power spectra shows the presence of a dominant frequency for each of the fluid points with numerous harmonics. The dominant frequencies for (a) to (d) are, respectively, 48.8, 63.5, 17.1, and 29.3 Hz, corresponding to the Strouhal numbers of St = 1.45, 1.88, 0.51, and 0.87. It appears that the fluid frequencies depend on location, with the lowest value occurring at or near $x/L = 0.5$, which corresponds to the middle of the membrane. These frequencies are not uncommon in fluid mechanics. According to Ho and Huerre (1984), the Strouhal number in circular jets is between 0.25 and 0.5.

The power spectrums of the unsteady membrane deflections, as seen in the right plots of Fig. 7, are reminiscent of a well-defined vibration of solids. A fundamental frequency and two harmonics are visible in the figure. The fundamental frequencies for (1) to (4) are, respectively, 0.220, 0.220, 0.195, and 0.171 Hz, corresponding to St = 0.0065, 0.0065, 0.0058, and 0.0051. Obviously, these low frequencies do not resonate with the higher fluid frequencies. Although the membrane could have exerted an influence on the sensitive shear layer separation near the leading edge, it appears that for the values of parameters used in this investigation, this influence is minimal.

8.4. Vortex generation

Attention is next turned to Fig. 8 where flow field over the flexible membrane is presented in terms of vorticity contours for Re = 38 416 at 10° and 40°. For the present two-dimensional flow, the vorticity vector is perpendicular to the plane of the figure. The local clockwise rotation of fluid element represents a negative vorticity with the vorticity vector pointing into the plane of the figure, while the counterclockwise rotation is positive and pointing outward. The range of contour values in this figure is from −6000 (blue in electronic version of the paper) to +6000 (red). The membrane chord is positioned horizontally while the flow is approaching the membrane from the left with an angle of 10° and 40° below the chord line. For both frames in this figure, the prestrain value is zero.

For 10° angle of attack, a boundary layer develops smoothly along the membrane and separates beyond the point of maximum camber. The vorticity generated at the leading edge slowly diffuses across the boundary layer until the boundary layer separates from the membrane. The shear layer, which is marked with a large concentration of negative (clockwise) vorticity, runs nearly parallel to the chord line. A large recirculation region is formed between the membrane and the shear layer. The boundary layer formed below the membrane is highly concentrated with positive (counterclockwise) vorticity, which remains intense until the boundary layer arrives at the trailing edge. At the trailing edge, the intense positive vortex just below the trailing edge rises and interacts with the detached shear layer from

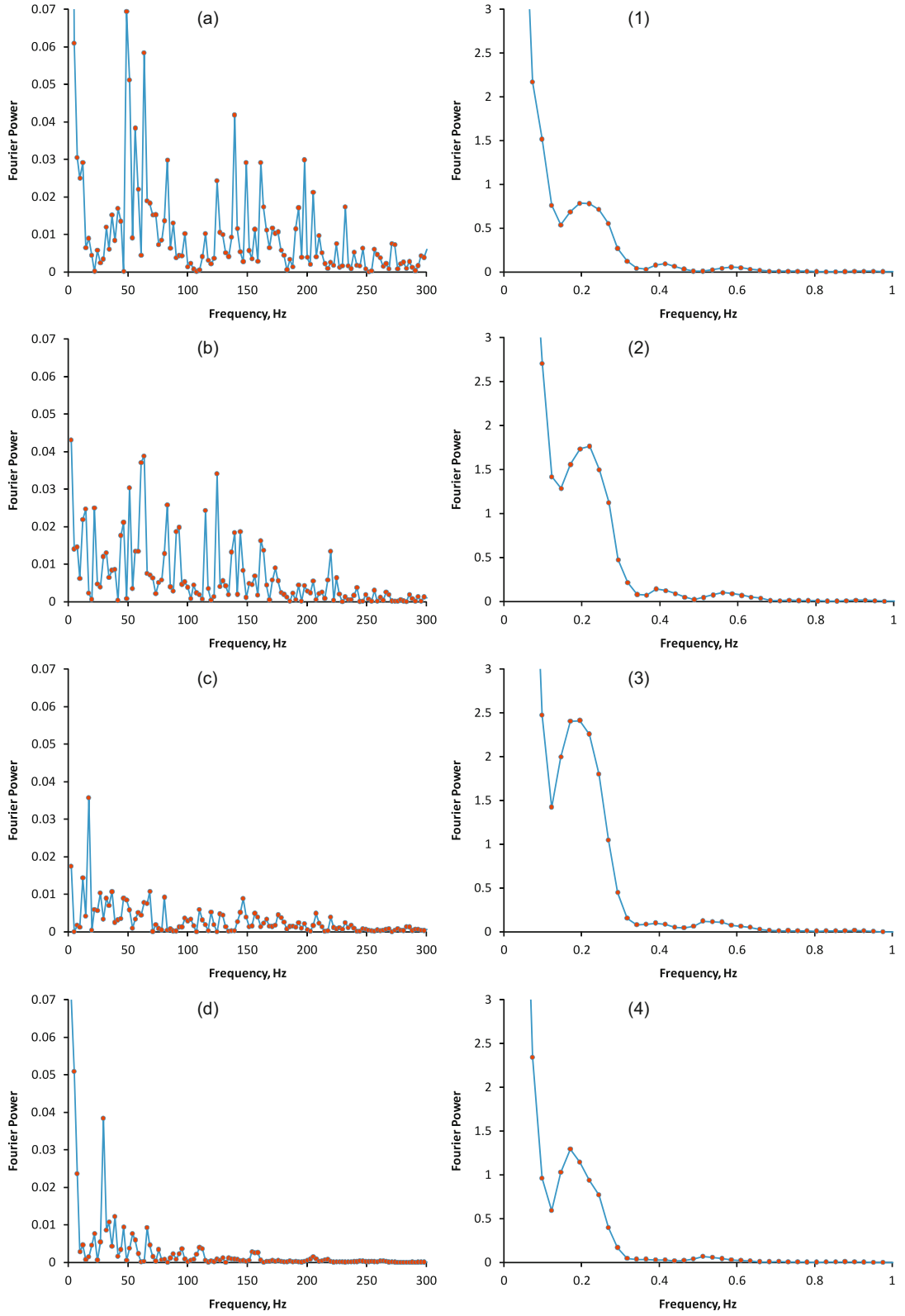

Fig. 7. Fourier power spectrum for the fluid (left) and membrane (right); Re = 38,426, angle of attack 40°, zero prestrain; the control points in air were positioned at (a) $(x/L,y/L) = (0.147,0.112)$, (b) (0.271,0.152), (c) (0.5,0.191), and (d) (0.748,0.184); the control points of (1–4) were on the membrane at the same values of x/L.

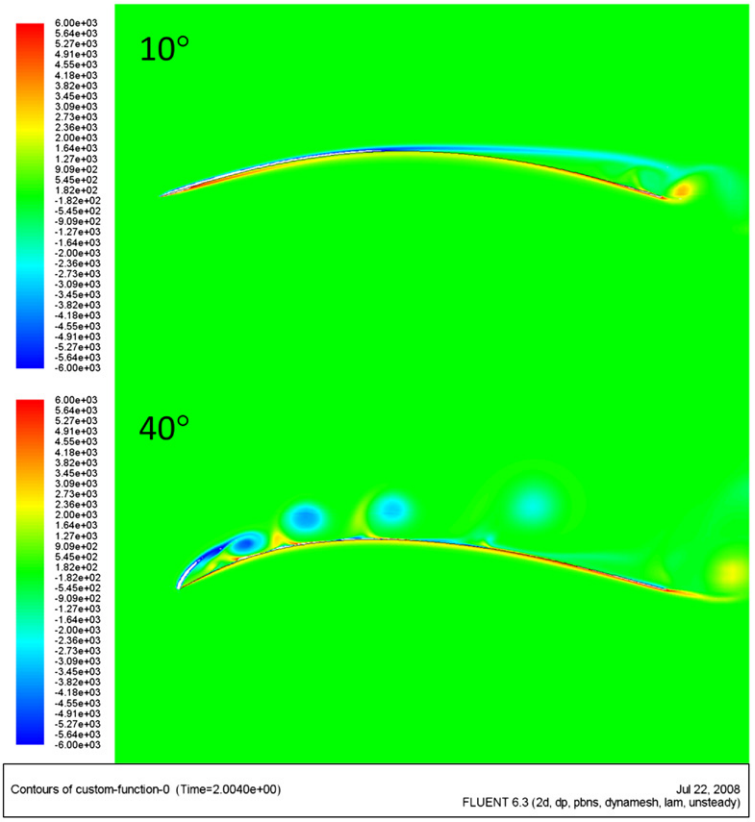

Fig. 8. Vorticity contours for flow over the flexible membrane; the contours are plotted for Re = 38 416, $\alpha = 10^\circ$ (top) and 40° (bottom), zero prestrain, 99 contour levels from $\omega = -6000$ (blue) to $+6000$ (red), and time step 1×10^{-4} s. The shear layer is closer to the membrane at lower angle of attack. The shear layer moves away as the angle of attack is increased, leading to vortex generation and roll-up above the membrane. (For interpretation of the references to colour in this figure legend, the reader is referred to the web version of this article.)

above. This interaction between positive and negative vortices results in a downstream vortex shedding and does not have a noticeable oscillatory effect on the membrane, as confirmed by Fig. 6.

For 40° angle of attack, the flow above the membrane is quite different. As seen in the lower frame of Fig. 8, flow separates at the leading edge, forming a small separation region. The flow emerging from the leading edge has an intense negative vorticity that does not allow the shear layer to remain attached to the membrane. As seen in the figure, the shear layer breaks into an intense vortical flow that detaches from the shear layer and travels downstream along the upper surface of the membrane. The shedding and roll-up of these vortices sets the membrane into oscillations, as revealed earlier in Fig. 6.

Fig. 9 presents a time sequence of the flow field at 40° angle of attack. A number of interesting events are noticeable in the figure. The clearest message of the figure is that the flow here is marked with frequent generation of leading edge vortices that prevent the formation and growth of a well-defined boundary layer. Positive vorticity is not limited to the lower surface of the membrane. Here, there are intermittent regions of positive (counterclockwise) rotation above the membrane. These regions of positive vorticity are created by the interaction of the negative leading edge vortices with the membrane surface. A negative vorticity forces the air to move upstream near the surface (reverse flow), and this localized upstream motion creates the positive vortical motions seen in red color near the surface.

Careful review of the vorticity frames in Fig. 9 reveals an interesting interaction among the vortices. If we follow the motion of the vortex located near $x/L = 0.3$ in the first frame, which has a negative vorticity and thus rotates clockwise, in frames 2 and 3 it approaches a pair of negative vortices that are merging. In frames 4–10, this vortex merges with the aforementioned pair and leaves the membrane as a large negative vortex. Interestingly, there is a similar isolated vortex in frame 11, approximately in the same location as the previous vortex. Following this vortex

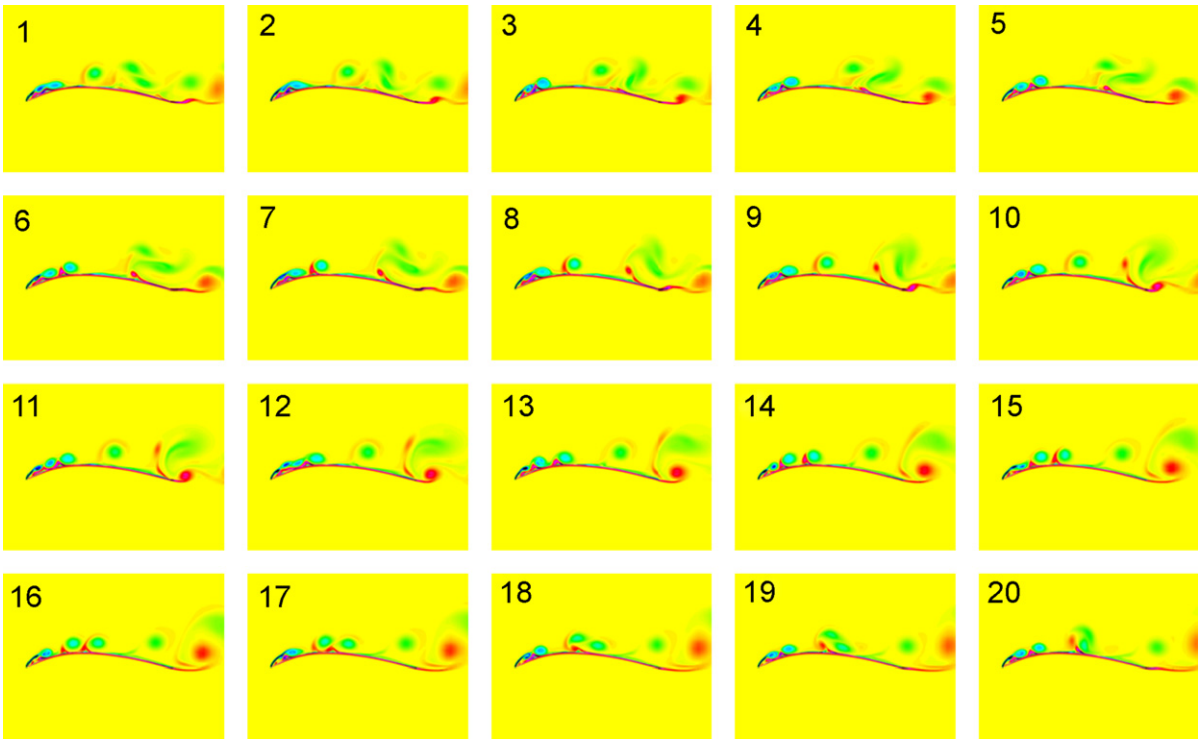

Fig. 9. Vorticity contours for flow over the flexible membrane; the contours are plotted for Re = 38 416, $\alpha = 40^{\circ}$, zero prestrain, 99 contour levels from $\omega = -5000$ (blue) to $+5000$ (red), time step 1×10^{-4} s, animated every 20 time steps, 0.002 s between the frames. The shear layer is detached from the membrane, and the vortex generation and roll-up are visible above the membrane. (For interpretation of the references to colour in this figure legend, the reader is referred to the web version of this article.)

in frames 11–20 shows that it does not merge with any other vortex and manages to escape the vortex system unaltered.

Flow below the membrane in Fig. 9 is rich with positive vorticity concentrated in a thin boundary layer near the surface. There is no evidence of any vortex formation below the membrane. However, the intense positive vorticity in this region leads to the formation of a large trailing edge vortex. The trailing edge vortex meets the multiple leading edge vortices at the trailing edge, resulting in a complex vortex shedding behind the membrane. It is this complex vortical and oscillatory flow that sets the membrane into oscillations, as it was observed earlier.

8.5. *Flexible verus rigid membrane*

The importance of flexibility and oscillation in the aerodynamic performance of the membrane is seen in Fig. 10 where time sequences of flow fields are presented for the flexible (1A–4A) and rigid (1B–4B) membranes. As the vortices travel downstream, they gradually lose their intensity due to vorticity diffusion, and they gradually fade away. The flow fields for the flexible and rigid membranes are very similar as far as the vortical flow is concerned. However, careful examination of the separation region shows that the vortices of the rigid membrane are farther away from the membrane. It appears that the oscillations of the flexible membrane attract the vortices, bringing them closer to the membrane, and the membrane rigidity repels them, making the recirculation zone larger. This indicates that the size of the recirculation region for the flexible membrane is smaller. The smaller size of the recirculation region for the flexible membrane is also confirmed experimentally by the smoke flow visualizations of Rojratsirikul et al. (2008). This suggests that flexible membranes might have a lower drag coefficient and higher lift coefficient, leading to a delayed stall and a better aerodynamic performance compared to the rigid membrane.

The aforementioned benefits of membrane oscillations due to flexibility diminish as the angle of attack is decreased. Fig. 11 presents the snapshots of the flow for different angles of attack. The membranes in the left frames are flexible, while those in the right frames are rigid. At 10°, the shear layer is close to both flexible and rigid membranes, and there

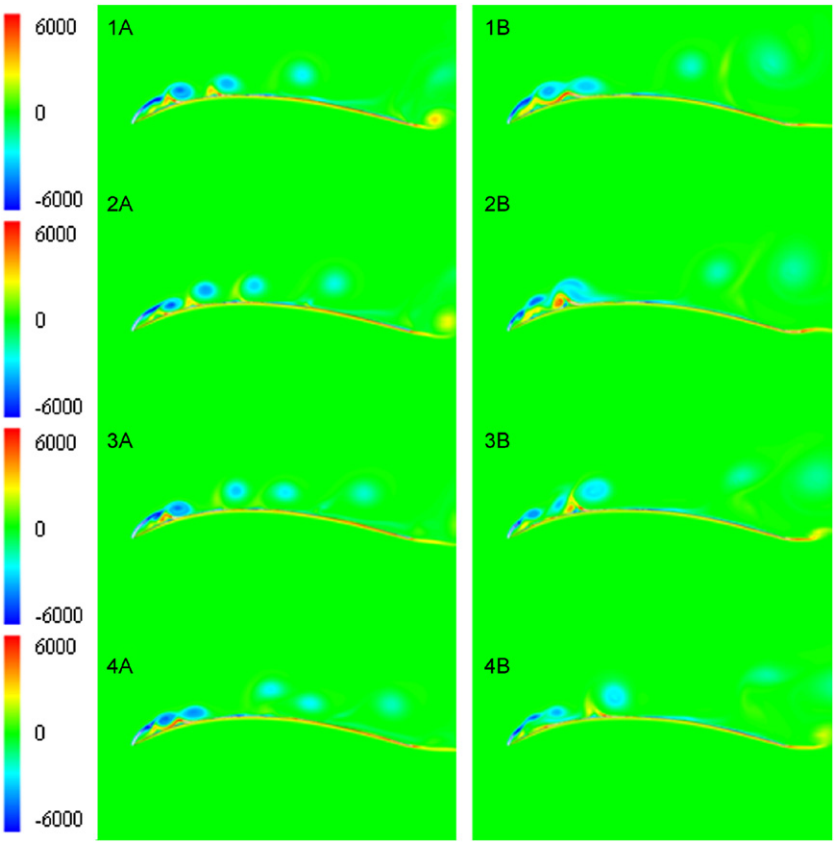

Fig. 10. Vorticity contours for flow over the flexible (left) and rigid (right) membranes; the contours are plotted for Re = 38 416, $\alpha = 40^{\circ}$, zero prestrain, 99 contour levels from $\omega = -6000$ (blue) to $+6000$ (red), and time step 1×10^{-4} s. The time between frames is 0.004 s. The flow fields of the flexible and rigid membranes have many similar features. However, the sizes of the separation and recirculation zones are smaller for the flexible membrane. (For interpretation of the references to colour in this figure legend, the reader is referred to the web version of this article.)

is no sign of vortex roll-up on the membrane surface. At higher angles of attack, vortex roll-up is visible in the figure and the oscillations of the flexible membrane become more effective in shrinking the size of the separation zone. This is also confirmed by the visualization photographs of Rojratsirikul et al. (2008), which indicate that the size of the recirculation region becomes progressively smaller as the angle of attack is increased.

As a complement to the vorticity patterns of Figs. 10 and 11, four sample streamline plots are presented in Fig. 12. The figure contains streamlines for low and high values of Re, flexible and rigid membranes, and zero and non-zero prestrains. The flexible membrane in plot (1) shows a smaller separated region as compare to that of the rigid membrane in plot (2). As seen in the figure, the vortex after the midpoint of the membrane and the detached vortex just downstream of the trailing edge are larger for the rigid membrane. Moreover, the streamlines above the membrane have moved away, confirming a larger separation region for the rigid membrane.

Earlier, in Fig. 6, it was noticed that membrane fluctuations are larger at low Re, especially at high prestrains. As seen in Fig. 12 (3), larger vortices roll on the membrane in the case of low Re and high prestrain. Under such conditions, the membrane is subjected to higher pressure fluctuations due to vortex roll-ups; considering the lower tension of the membrane in this case (compared to high Re case), the membrane fluctuations are larger. For the case of high Re seen in Fig. 12 (4), the membrane has a large deformation and tension; although the membrane has responded to the high fluid velocity by a large deformation, it is less responsive to the transient behavior of the separation region due to higher tension.

One possible explanation as to why the separation region of the flexible membrane becomes smaller with the angle of attack compared to the rigid wing may be presented based on the flux of vorticity from the membrane into the fluid. The z-component of vorticity, ω_z, may be imparted into the fluid by the streamwise pressure gradient, $\partial p/\partial x$, and the local streamwise acceleration of the membrane, $\partial u/\partial x$ (Panton, 2005). The first component, namely $\partial p/\partial x$, is present in both flexible and rigid membranes, but its magnitude is somewhat different for the two membranes. The second component,

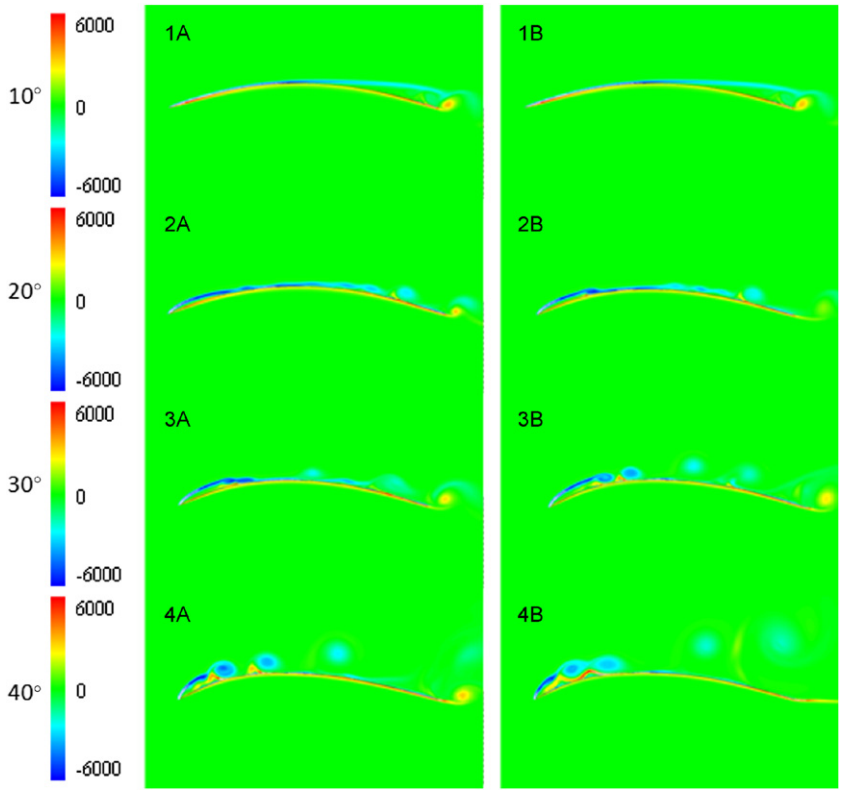

Fig. 11. Vorticity contours for flow over the flexible (left) and rigid (right) membranes; the contours are plotted for Re = 38 416, $\alpha = 10$–40°, zero prestrain, 99 contour levels from $\omega = -6000$ (blue) to $+6000$ (red), and time step 1×10^{-4} s. The effect of membrane flexibility on reducing the size of the separation and recirculation zones is enhanced with the angle of attack. (For interpretation of the references to colour in this figure legend, the reader is referred to the web version of this article.)

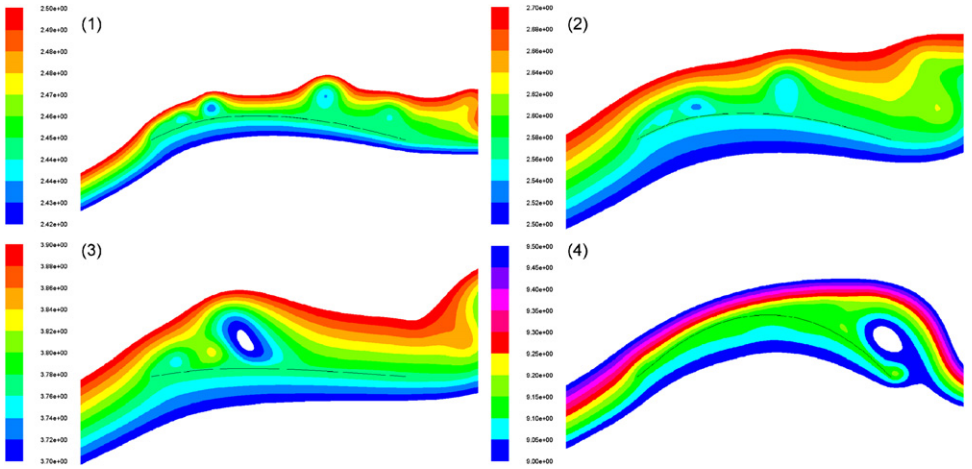

Fig. 12. Streamlines for the flexible and rigid membranes at 40° angle of attack; the number of streamlines for each plot is 10; (1) Re = 38 416, flexible, zero prestrain; (2) Re = 38 416, rigid; (3) Re = 38 416, flexible, 0.074 prestrain; (4) Re = 141 500, flexible, zero prestrain.

namely $\partial u/\partial x$, is present only in the flexible membrane, because it oscillates. Since the membrane camber changes with the angle of attack, the influence of both $\partial p/\partial x$ and $\partial u/\partial x$ changes the flux of vorticity. The contributions of these two components to fluid vorticity could be positive or negative, depending on the nature of pressure and velocity variation

along the membrane. The overall effect is a shear layer closer to the surface and a smaller recirculation zone at higher angles of attack.

9. Concluding remarks

This paper describes a detailed computational and analytical study of the response of prestrained flexible membranes to airflow at different angles of attack. The flow Reynolds number was lower than that normally considered for rigid airfoils in aerospace applications. The combination of low Reynolds number, high angle of attack, and different levels of prestrain made the outcome of this work more relevant to the aerodynamics and design of the compliant membranes employed in micro air vehicles (MAV) and the wings of flying mammals, such as bats.

The computations indicated that a prestrained membrane has smaller deflection. A membrane with less prestrain is more responsive to aerodynamic loading. This is also confirmed by the analytical solution for a deflection under constant pressure difference. It is further found that the membranes are often deflected in airflow asymmetrically. The higher Reynolds number generally gives a more symmetric deformation, while the higher values of prestrain at lower Re lead to higher asymmetry. Angle of attack also contributes to the asymmetry of the deformations. At low Reynolds numbers, the lift coefficient increases monotonically with the angle of attack. At higher Reynolds number, however, the lift coefficient increases up to a certain angle of attack, beyond which it decreases.

In response to airflow, the membrane oscillates in the streamwise and vertical directions. The streamwise oscillations change the instantaneous symmetry of the membrane, while the vertical motion affects the camber. At the higher Reynolds number, the amplitudes of oscillations are relatively small, and the point of maximum camber is close to the middle of the membrane. For the lower Reynolds number, on the other hand, the oscillations occur in wider amplitude. In this case, the largest amplitude of oscillations occurs at the higher prestrain and higher angle of attack. The low-Re oscillations are predominantly streamwise with small vertical amplitudes of oscillations.

At low Reynolds number and low angle of attack, the flow develops over the surface of the membrane and separates downstream beyond the point of maximum camber. Vortices are not seen above or below the membrane, but there is a strong vortex shedding at the trailing edge. At higher angle of attack, however, the flow is characterized by frequent formations of leading edge vortices. The flow above the membrane is mainly comprised of multiple vortices which are initiated at the leading edge of the membrane. These vortices grow larger and frequently interact and mix with the flow near the membrane surface. A single vortex generated at the tip of the membrane can approach and merge with other vortices, or alternatively it may escape the vortex region unchanged and without merging.

The shear layer is closer to the membrane at smaller angles of attack and moves away as the angle of attack is increased. The flexible membrane has a smaller recirculation region compared to rigid membranes, which may delay the stall and lead to a better aerodynamic performance of the flexible membrane.

Acknowledgment

This research was carried out when the lead author was a visiting professor at Brown University, supported by a sabbatical leave from Southern Illinois University Edwardsville.

References

Galvao, R., Israeli, E., Song, A., Tian, X., Bishop, K., Swartz, S., Breuer, K., 2006. The aerodynamics of compliant membrane wings modeled on mammalian flight mechanics. 36th AIAA Fluid Dynamics Conference, Paper 2006-2866, pp. 11–22.

Gordnier, R.E., 2008. High fidelity computational simulation of a membrane wing airfoil. 46th AIAA Aerospace Sciences Meeting and Exhibit, Paper AIAA 2008-614, 7–10 January, Reno, Nevada, USA.

Greenhalgh, S., Curtiss Jr., H.C., 1986. Aerodynamic characteristics of a flexible membrane wing. AIAA Journal 24, 545–551.

Hedenstrom, A., Johansson, L.C., Wolf, M., von Busse, R., Winter, Y., Spedding, G.R., 2007. Bat flight generates complex aerodynamic tracks. Science 316, 894–897.

Hein, B.R., Chopra, I., 2007. Hover performance of a micro air vehicle: rotors at low Reynolds number. Journal of the American Helicopter Society 52, 254–262.

Ho, C.M., Huerre, P., 1984. Perturbed free shear layers. Annual Review of Fluid Mechanics 16, 365–424.

Katz, J., Plotkin, A., 2001. In: Low-Speed Aerodynamics second ed. Cambridge University Press, Cambridge.

Kreyszig, E., 1991. In: Differential Geometry. Dover, Mineola, New York.

Lian, Y., Shyy, W., 2005. Numerical simulations of membrane wing aerodynamics for micro air vehicle applications. Journal of Aircraft 42, 865–873.

Liang, S.J., Neitzel, G.P., Aidun, C.K., 1997. Finite element computations for unsteady fluid and elastic membrane interaction problems. International Journal for Numerical Methods in Fluids 24, 1091–1110.

Mateescu, D., 2003. Analysis of aerodynamic problems with geometrically unspecified boundaries using an enhanced Lagrangian method. Journal of Fluids and Structures 17, 603–626.

Panton, R.L., 2005. In: Compressible flow 3rd ed. Wiley, New Jersey.

Perry, A.E., Chong, M.S., 1980. Fluid flow studies using a stretched membrane: analogue solution of the flow equations and experimental measurement of wall pressure distribution. Journal of Physics E: Scientific Instrumentation 13, 575–578.

Rojratsirikul, P., Wang, Z., Gursul, I., 2008. Unsteady aerodynamics of membrane airfoils. 46th AIAA Aerospace Sciences Meeting and Exhibit, Paper AIAA 2008-613, Reno, Nevada, USA.

Shyy, W., Ifju, P., Viieru, D., 2005. Membrane wing-based micro air vehicles. Applied Mechanics Review 58, 283–301.

Shyy, W., Udaykumar, H.S., Rao, M.M., Smith, R.W., 2007. In: Computational Fluid Dynamics with Moving Boundaries. Dover, Mineola, New York.

Smith, R., Shyy, W., 1996. Computation of aerodynamic coefficients for a flexible membrane airfoil in turbulent flow: a comparison with classical theory. Physics of Fluids 8, 3346–3353.

Song, A.J., Breuer, K.S., 2007. Dynamics of a compliant membrane as related to mammalian flight. 45th AIAA Aerospace Science Meeting 12, Paper 8076–8085.